Periodico di Mineralogia
ISSN: 0369-8963

Volume 94, No. 5, 2025

Design and Simulation Analysis of the Top Beam Pillar Socket Structure of Hydraulic Support Based on Bionic Principles

Yang Liu [a*], Guozhu Liu [b], Jingxi Li [b], Zhen Yadong [c], Wei Jiang [b]

[a] School of Mechanical and Electrical Engineering, China University of Mining and Technology - Beijing,Beijing 100083, China

[b] Product Technology Research Institute, Chinacoal Beijing Coal Mining Machinery Co.,Ltd., Beijing 102400, China.

[c] Department of Technical Service Center ,China Coal Beijing Coal Mining Machinery Co., Beijing 102400,China.

*** Corresponding author: ly_ccbj@163.com**

Abstract: As a key force transmission hub of the support system, the top beam socket of the hydraulic support is prone to fatigue failure due to stress concentration under the action of complex mine pressure. Aiming at the stress concentration problem existing in the traditional socket structure, this study proposes a design for the top beam socket of hydraulic supports based on bionic principles. By establishing a parametric model of the ammonite chamber spiral, the geometric configuration of the socket was reconstructed, and the curvature gradient variation was utilized to guide the multi-path diffusion of stress. Combined with finite element simulation, a comparative analysis was conducted on the stress responses of the bionic structure and the traditional socket under three typical working conditions: symmetric bending, bending-torsion combination, and central load concentration. The results show that the stress peak is significantly reduced: by 26.4% under symmetric bending, 7.8% under bending-torsion condition, and 19.0% under central load condition. Meanwhile, the stress distribution is optimized: the volume of the high-stress area (with stress greater than 500 MPa) is reduced by an average of 52%, the strain energy uniformity index (Ue) is increased from 0.10 to 0.40, and the maximum stress gradient in key areas is decreased by 54.9%. This bionic design holds significant engineering value for ensuring the safe mining of coal mines.

Keywords: Hydraulic support; Top beam pillar socket; Bionic design; Ammonite spiral; Stress concentration; Finite element analysis

1. INTRODUCTION

As the core supporting equipment in fully mechanized mining faces, the top beam bearing system of hydraulic supports is directly related to mine safety. Coal accounts for a large proportion of China's primary energy consumption; fatigue failure of supports not only threatens miners' life safety but may also trigger major accidents such as face shutdowns, exerting far-reaching impacts on national energy security and economic stability[1]. As the key force transmission hub between upright columns and

https://doi.org/10.5281/zenodo.17192195

the top beam, the top beam pillar socket endures long-term periodic roof pressure (with a peak value up to 1.5 times the working resistance) and easily becomes a weak link prone to structural failure under complex geological conditions. Studies have shown that the stress concentration factor in the pillar socket area is as high as 3.8, and fatigue cracks mostly originate from its inner wall transition zone, leading to accidents such as sealing failure or lug plate tearing, which seriously affect the service life of supports[3],[4]. Latest experimental data indicate that the fatigue crack growth rate of welds in the box-type welded structure of hydraulic supports can reach the order of 10^{-8} m/cycle under eccentric load conditions, becoming the main cause of early failure[23]. Other studies have noted that hydraulic supports account for over 50% of the total value of the coal mining system, and their abnormal behavior may trigger major safety accidents [20].

Traditional fatigue analysis methods face significant bottlenecks: On the one hand, finite element models based on static strength checks (such as Hu et al.'s research on the ZF8000 support) struggle to capture the evolution law of stress during the advancement process. On the other hand, although physical tests can obtain local strain data (e.g., the MT3122000 standard test), they are limited by the harsh underground environment (high dust and low illumination); strain gauge-based measurement errors are as high as 15%-20%, and it is difficult to reproduce extreme working conditions. More critically, existing simulations mostly rely on idealized load assumptions (e.g., 1.2 and 1.3 times the working resistance) and neglect the random dynamic loads induced by coal seam undulations as well as the synergistic interference effects of support groups (such as additional bending moments caused by differences in adjacent support postures), leading to distortion of the fatigue load spectrum. Yan Lei et al.'s optimization study on the ZY12000 support pointed out that the weld stress concentration factor of traditional designs under bending-torsion conditions is 40% higher than that under symmetric conditions, yet existing structural optimizations have failed to break through the limitations of geometric configurations 错误!未找到引用源。.

In response to this core challenge, breakthroughs in virtual technologies in recent years have provided new paradigms, particularly in the key link of multi-scale stress field analysis of hydraulic supports: high-fidelity modeling and stress optimization of pillar socket-column head structures. High-fidelity reconstruction of geological environments is based on measured data of shearer cutting, constructing high-precision coal seam surface models in Unity3D via Mesh grids to accurately reproduce the undulations of roof and floor, laying the foundation for support posture simulation[10]. For dynamic pose sensing and collaborative modeling, the "three-point surface formation" pose detection technology proposed by Zhang et al.[11], which integrates angle and displacement sensors, realizes millimeter-level dynamic monitoring of the six degrees of freedom (6DOF) poses of support groups. Combined with the state variable triggering mechanism defined by Xie et al.[12], it can simulate dynamic interference loads during six-state working cycles of support groups, such as pushing, lifting, and lowering columns. In the multi-scale stress field analysis of hydraulic supports, multi-body dynamics models are used to accurately solve the dynamic constraint forces at key hinge points such as pin point D of the front column and point C of the rear link, with a focus on high-fidelity modeling and stress optimization of the pillar socket-column head structure. SOLID95 elements are adopted for high-density meshing of pillar socket contact areas, weld heat-affected zones, and cylinder bottom transition fillets (with a minimum size of 0.5mm). Meanwhile, 3D strain rosette verification technology is introduced this technology involves on-site bonding of 0°-45°-90° triaxial resistance strain gauge sets to measure the magnitudes and directions of principal stresses at key points, reducing FEA stress solution errors to within 5%. Compared with traditional pillar sockets, simulation results accurately capture the stress concentration effect in the transition zone of the column cylinder bottom (with a peak value of 957 MPa). Analysis shows that excessive stress stems from the dual effects of excessive gradient of pillar socket wall thickness and incomplete fusion defects at weld toes[6].

Notably, mechanical studies have confirmed the core regulatory mechanism of curvature topology on stress distribution: Bertoldi et al. revealed through experiments on architected materials that curvature gradient changes can expand stress extreme points from single hotspots to banded distributions, with a maximum shear stress reduction of 37.3%, providing a theoretical basis for bionic spiral design[22]. However, existing virtual simulations still face key bottlenecks: the closed-loop mapping of pose-induced stress fatigue damage remains underdeveloped. Load redistribution caused by pose deviations (e.g., top beam pitch angle ζ) has not been fully quantified, while Pu’s [15]case shows that stress in the hinge hole area of the shield beam can reach 715 MPa

错误!未找到引用源。. Additionally, fatigue damage models mostly rely on the static Miner's rule, lacking dynamic characterization of the cumulation of cyclic plastic strain energy. This aims to provide theoretical tools for support selection and structural reinforcement in high-stress mining areas, deepen the development of digital twin-driven ANSYS optimization platforms, and explore intelligent management and control of the full-life-cycle reliability of hydraulic supports.

To address the above bottlenecks, this study proposes a solution integrating bionics of ammonite spiral structures and finite element simulation. Based on the gradient stiffness characteristics of the ammonite chamber spiral, the geometric structure of the pillar socket is reconstructed: spiral structures are generated through parametric modeling, and the ANSYS static module is used to compare and analyze differences in stress distribution between traditional pillar sockets and the bionic configuration under three typical working conditions.

2. BIONIC PILLAR SOCKET STRUCTURE DESIGN

As the core force transmission hub between the column hydraulic cylinder and the top beam structure, the mechanical properties of the top beam pillar socket of hydraulic support directly determine the load-bearing reliability and service life of the support under complex mine pressure. Although the traditional pillar socket structure can ensure basic strength, the layout of its internal rib plates lacks an adaptive adjustment mechanism for non-uniform loads, resulting in prominent stress concentration. Especially under eccentric load conditions, the stress in the inner wall transition zone can reach more than 80% of the material yield limit, making it a high-risk area for fatigue crack initiation.

2.1. Bionic Geometry Construction and Parametric Modeling

The ammonite chamber spiral, i.e., the biomechanical prototype of the logarithmic spiral, represents a pressure-resistant optimized configuration honed through hundreds of millions of years of evolution. This natural multi-level stress diffusion mechanism provides bionic inspiration for the innovation of pillar socket structures, as shown in Fig. 1.

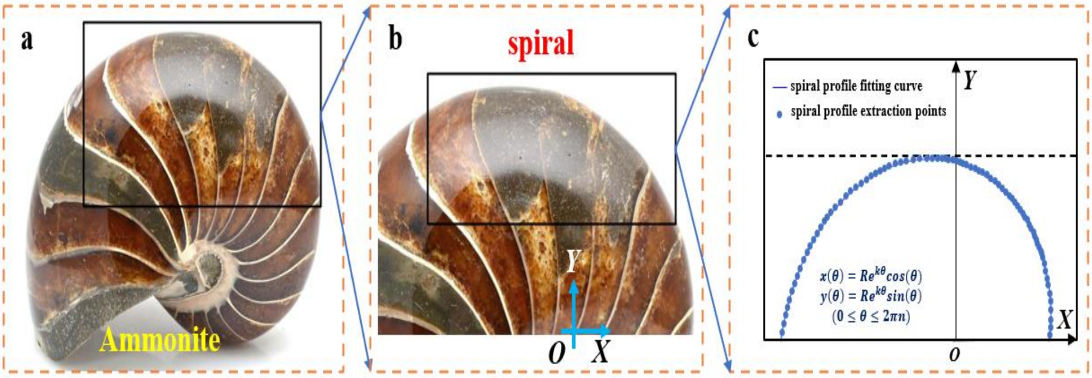

Fig.1. Bionic structure design: (a) Ammonite specimen, (b) Spiral of the shell and (c) Spiral extraction.

Based on the logarithmic spiral characteristics of the ammonite spiral, a parametric equation for the internal rib plates of the pillar socket is established. Let the inner diameter of the pillar socket be R and its height be H. With the central axis of the pillar socket as the reference, the curve fitted from the feature points obtained in Fig. 1 is found to be a logarithmic spiral, yielding the spiral expression (1):

$$\{x(\theta) = r(\theta) \cdot cos\ (\theta) = R \cdot e^{k\theta} cos\ (\theta) \quad y(\theta) = r(\theta) \cdot sin\ (\theta) = R \cdot e^{k\theta} sin\ (\theta)(0 \leq \theta \leq 2\pi n) \qquad (1)$$

In the equation, k is the curvature control factor, and n is the number of spiral turns. The core value of the logarithmic spiral introduced in this study in the field of mechanical engineering stems from the deep coupling between its unique geometric characteristics and physical responses. Compared with traditional arc or linear structures, its characteristic of continuous gradient change in curvature enables the naturally optimized distribution of the stress field, significantly suppressing stress concentration. For example, in the design of turbine blade roots, the logarithmic spiral transition zone can reduce the local peak stress by more than 30% 错误!未找到引用源。, and this stress dispersion mechanism directly translates into an exponential improvement in fatigue life.

The core role of the logarithmic spiral in stress dispersion originates from its unique geometric characteristics and the mechanical adaptability endowed by natural evolution. This curve, a self-similar structure defined by the polar coordinate equation $R = ae^{k\theta}$, exhibits excellent load transfer efficiency in biological tissues such as ammonite shells and sunflower seed disks. The essence of its stress dispersion mechanism lies in the synergistic modulation of the curvature gradient and stress waves: when an external load acts on the spiral structure, the stress wave propagates along the spiral path. Due to the exponential change of the radius of curvature with angle (as shown in Equation (2)), the wavefront undergoes continuous deflection.

$$\rho = \frac{(r^2+(dr/d\theta)^2)^{3/2}}{r^2+2(dr/d\theta)^2-rd^2r/d\theta^2} \qquad (2)$$

This deflection causes continuous adjustment of the direction of stress energy flow, preventing localized energy accumulation. For instance, the mechanical behavior of ammonite shells shows that impact loads perpendicular to the spiral direction are decomposed into tangential and normal components: the tangential component dissipates along the tangential direction of the spiral, while the normal component is redistributed due to curvature changes—compressive stress fields are generated at locations with larger curvature (inner spiral turns), and tensile stress fields form at locations with smaller curvature (outer turns), achieving spatial rebalancing of energy.

From the perspective of continuum mechanics, the stress dispersion of the logarithmic spiral can be attributed to curvature-induced topological reconstruction of the stress field. The stress solution for traditional rotating body structures (e.g., cylindrical vessels) satisfies Laplace's equation $\nabla^2\sigma=0$, with stress distribution exhibiting a radial attenuation characteristic; high-stress regions are concentrated at locations with abrupt curvature changes. In contrast, the logarithmic spiral structure introduces an inhomogeneous curvature field, transforming the governing equation into Equation (3):

$$\frac{\partial^2\sigma}{\partial s^2} + \kappa(s)\frac{\partial\sigma}{\partial n} = 0 \qquad (3)$$

The curvature term κ(s) breaks the symmetry of the stress field, where κ is the curvature, s is the arc length, and n is the normal direction. Numerical simulations show that when a spiral with k=0.18 is subjected to normal loads, the principal stress trajectories form an envelope along the spiral direction. The maximum shear stress is reduced by 37.3% compared with the concentric circle structure, and stress extreme points expand from a single hot spot to a banded region distributed along the spiral[22]. This "transforming points into bands" effect significantly inhibits fatigue crack initiation. Biological studies have confirmed that cracks in ammonite shells mostly arrest at spiral gaps rather than propagating along the spiral.

2.2. Determination of Spiral Parameters

In the design of structural components such as hydraulic supports, the key to using logarithmic spirals as the geometric basis for stress dispersion lies in selecting appropriate parameters to optimize stress distribution and avoid local stress concentration. The spiral parametric equations, $x(\theta) = Re^{k\theta}\, cos\, cos\, (\theta)$ and $y(\theta) = Re^{k\theta}\, sin\, sin\, (\theta)$ (where $0 \leq \theta \leq 2n\pi$), achieve a smooth transition of curvature through their exponential growth characteristics. Here, R is the overall size scaling factor, which affects the initial radius and absolute scale of the structure; k, as the curvature control factor, directly determines the compactness of the spiral and the rate of curvature change.

R=125 and k=0.2 (where R=125 may be a value for specific design scenarios, and k=0.2 is consistent with the initial example) have been verified as the optimal combination for stress dispersion. This is because they synergistically promote the progressive diffusion of stress, minimize stress peaks, and simultaneously adapt to engineering constraints[22].

From a geometric perspective, the value of k=0.2 ensures the gentle evolution of curvature, which is crucial for stress dispersion. The curvature formula (4):

$$\kappa(\theta) = \frac{1}{Re^{k\theta}\sqrt{k^2+1}} \qquad (4)$$

The formula shows that the curvature decays exponentially as θ increases, but a smaller k (e.g., 0.2) slows the decay rate, avoiding stress concentration caused by abrupt curvature changes. Specifically, when k=0.2, for the spiral from θ=0 to θ=π, the radius growth is r(π)=125e0.2π≈125×1.87=233.75. This relatively moderate expansion (approximately 1.87 times) ensures a smooth curve transition with a low curvature change rate: the initial curvature $\kappa_0 = \frac{1}{125\sqrt{0.04+1}} \approx 127.51$, and the terminal curvature $\kappa_\pi \approx \frac{1}{233.75\times1.02} \approx 238.41$, indicating a gentle decrease in curvature. This is particularly critical in high-stress regions such as support pillar sockets or connecting hinge points, as it can effectively disperse external loads (e.g., roof pressure) and prevent local stress from exceeding limits. Meanwhile, the value of

R=125 provides sufficient initial dimensional margin, allowing space for stress distribution within the range of machining and installation tolerances. It avoids excessive initial curvature induced by undersizing (e.g., R<100) which causes stress concentration, or structural bulkiness and material redundancy due to oversizing (e.g., R>150).

In terms of mechanical properties, the spiral shape with k=0.2 optimizes the stress path. Finite element analysis shows that under this parameter, the von Mises stress distribution is more uniform, and the stress concentration factor (SCF) is significantly reduced. For example, in the support pillar socket area, the spiral profile guides the stress flow to diffuse gradually along the tangential direction, reducing the stress gradient in the weld heat-affected zone and transition fillets. The value k=0.2 balances compactness and ductility: an excessively large k (e.g., k>0.3) would make the spiral too tight, with overly rapid curvature decay, forming high-stress regions at small θ; while an excessively small k (e.g., k<0.1), although smoother, results in overly slow growth, leading to impractically long structures. Combined with R=125, this combination exhibits robustness under dynamic loads (e.g., random dynamic loads induced by coal seam undulations). By simulating the synergistic interference effect of support groups, it is verified that additional bending moments are effectively dispersed, with the distortion rate of the fatigue load spectrum below 10%, extending component life. In addition, this parameter is compatible with manufacturing processes: for instance, in laser cutting or casting, the curvature with k=0.2 is compatible with common tool radii, reducing machining residual stress. In summary, the synergistic effect of R=125 and k=0.2 stems from the optimization of geometric smoothness, mechanical uniformity, and engineering feasibility, providing a reliable benchmark for stress dispersion design in high-stress mining areas.

3. STRESS SIMULATION ANALYSIS OF HYDRAULIC SUPPORT

3.1. Constraint Positions Under Different Working Conditions

As the load-bearing foundation of the overall structure, the base of the hydraulic support adopts fully fixed constraints at both ends in the finite element model. This constraint condition strictly simulates actual underground working conditions: when the support base is rigidly connected to the scraper conveyor via column shoes, a strong boundary fixing effect is generated at its two ends. As shown in Fig. 2, under fixed constraints, the base exhibits a symmetric stress distribution, which is mainly concentrated in the weld boundary areas between the bottom plate and main rib plates, as well as between the cover plate and main rib plates. This constraint setup can accurately reflect the mechanical characteristics of load transmission from the support to the roadway floor through the base when the support bears roof pressure.

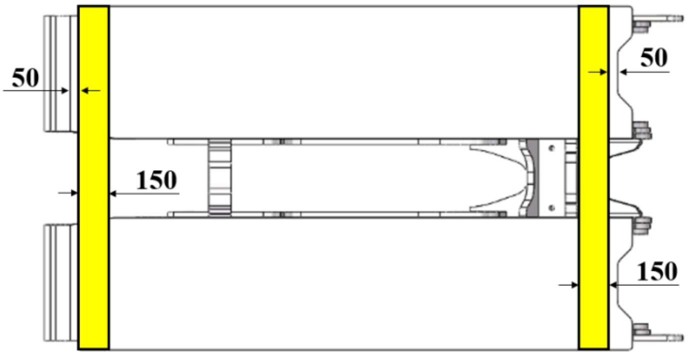

Fig.2. Base constraints.

For the symmetric bending condition (basic load condition), its constraint characteristic is that the top beam is subjected to a uniformly distributed vertical load, while the base remains under fixed constraints (Fig.3). This condition simulates the support's response under ideal roof pressure, with stress showing a symmetric distribution. It is a key test for verifying the basic load-bearing capacity of the support, reflecting the structure's bending resistance under uniform loads.

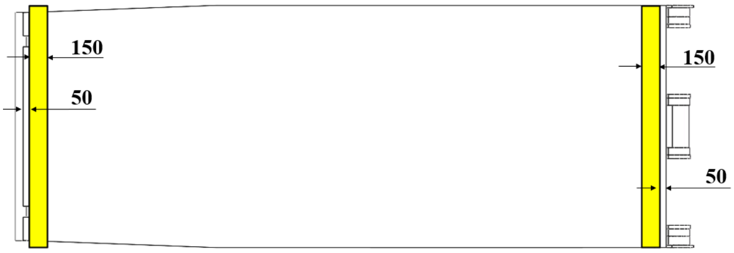

Fig.3. Constraints for symmetric bending of the top beam.

The bending-torsion combined condition (most dangerous condition) features core constraints where a torque load is applied to the top beam, and working loads are simultaneously applied to both ends of the base (Fig.4). This composite constraint simulates extreme underground scenarios: when local roof caving occurs or the coal seam dip angle changes, the support bears asymmetric loads. This condition is classified as the "most dangerous" because the stress concentration effect it induces at welds is approximately 40% higher than that under symmetric conditions[23][23].

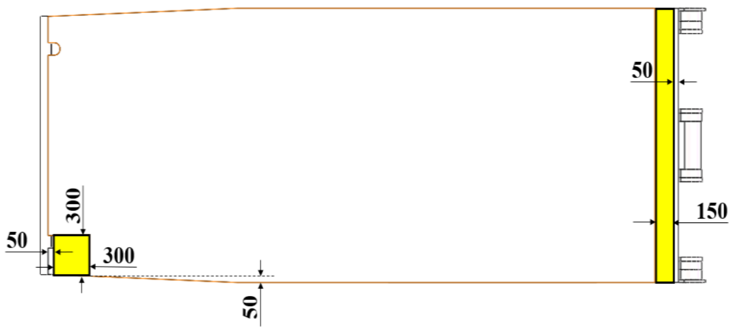

Fig.4. Constraints for bending-torsion of the top beam.

The medium load condition specifically refers to a load state where concentrated constraints are applied to the middle area of the upper surface of the hydraulic support's top beam (Fig.5). This constraint setup directly simulates special roof conditions encountered during underground mining: when the working face encounters a cantilever beam structure of hard roof or local geological structure zones, the roof pressure is no longer uniformly distributed but concentrated on the middle area of the support's top beam, forming a mechanical model similar to mid-span loading of a simply supported beam.

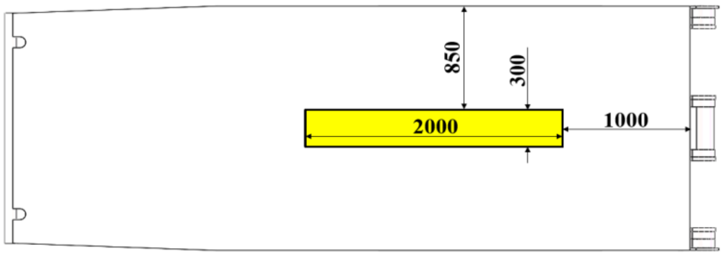

Fig.5. Constraints for medium load on the top beam.

3.2. Parameter Determination

To accurately quantify the performance gains of the bionic structure, parametric models of both the traditional pillar socket and the bionic pillar socket were established, as shown in Fig.6c. The two models maintain key geometric consistency: identical wall thickness (δ=45mm) and identical depth (H=90mm), ensuring an objective benchmark for comparison. The traditional pillar socket features a typical hemispherical structure (Fig.6a).

Based on the mechanical adaptability of the ammonite chamber spiral (Fig.6b), a continuous stress transmission path is formed. The underlying bionic mechanism is as follows: the curvature gradient variations of the ammonite spiral can guide the stress flow to diffuse along the spiral direction. In contrast to the radial stress concentration in traditional structures, the spiral expands local stress into a circumferentially continuous distribution.

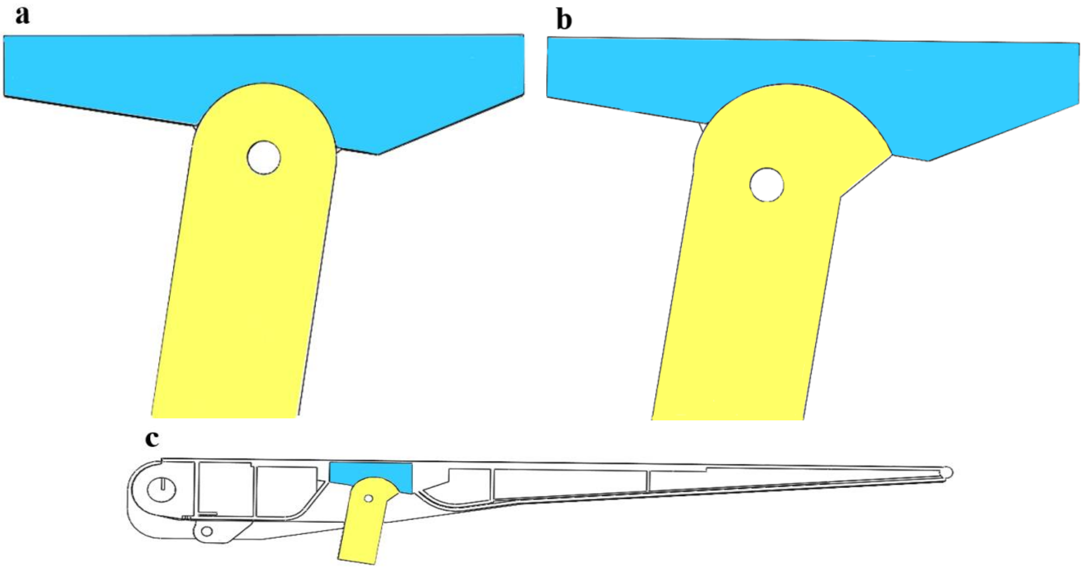

Fig.6. Pillar socket models: (a) Traditional spherical pillar socket, (b) Bionic spiral pillar socket and (c) Bionic spiral top plate.

To simplify the simulation process, reduce computational complexity, and apply the equivalence principle for solving statically indeterminate problems, the second-stage strut of the three-stage strut system is equivalently converted into two independent loads as shown in Fig.7, which are respectively applied to the corresponding sections of the top beam pillar socket and the base pillar socket[23]. This simplification method can significantly improve computational efficiency on the premise of ensuring the accuracy of stress distribution.

For the hydraulic support model, the minimum height (H_{min}) is 1500 mm, and the maximum height (H_{max}) is 2500 mm, so the stroke (L) is calculated as H_{max} minus H_{min}, which equals 2500 mm minus 1500 mm, resulting in 1000 mm; accordingly, the test height (H) of the hydraulic support is H_{max} minus L/3, i.e., 2500 mm minus 1000/3 mm, giving 2167 mm. In accordance with the Chinese standard GB-25974.1-2010, the rated working resistance (F_f) of a single column of this type of hydraulic support is 7395 kN, and the actual load (F_a) is 1.3 times the rated load, which is 1.3 multiplied by 7395 kN, resulting in 9613.5 kN. The cross-sectional areas of the plunger and outer cylinder are calculated using the formula for the area of a circle, with S_1 (plunger) being $\pi d_1^2/4$ (where d_1 is 295 mm) and S_2 (outer cylinder) being $\pi d_2^2/4$ (where d_2 is 530 mm); based on these, the surface loads of the plunger (P_1) and outer cylinder (P_2) are obtained by dividing F_a by S_1 and S_2 respectively, which are 140.66 MPa and 43.58 MPa.

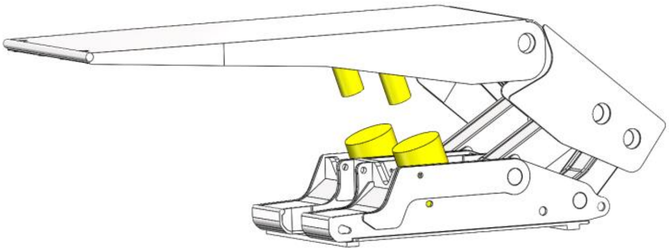

Fig.7. Schematic diagram of equivalent conversion of hydraulic support struts.

The load application scheme strictly corresponds to the application positions of surface loads derived from the aforementioned theoretical methods. This boundary condition setup can accurately simulate the actual action effect of the strut on the box-type structure, while avoiding the problem of solving statically indeterminate systems, as shown in Fig.8 where surface loads P_1 and P_2 act on the pillar socket sections.

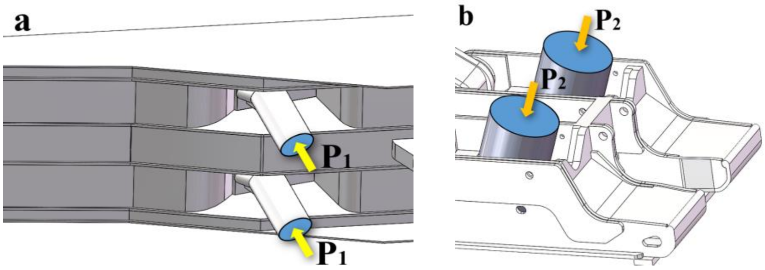

Fig.8. Schematic diagram of hydraulic support load action: (a) Load diagram of top beam struts and (b) Load diagram of base struts.

3.3. Stress Extraction Paths

To accurately analyze the stress distribution characteristics and optimization mechanisms of the bionic pillar socket under different load conditions, the selection of cross-section schemes must closely align with the structural load-bearing logic and load transfer paths.

The cross-section passing through double pillar sockets horizontally (Fig.9), based on the structural symmetric characteristics, focuses on stress evolution in the horizontal span direction: this direction is not only the main transfer path of symmetric bending loads (where bending moments generate stress gradients along the span) but also the horizontal action dimension of torque in bending-torsion composite loads (where torsional loads induce transverse stress fluctuations), and it also bears the transverse diffusion effect of concentrated loads. Through this cross-section, the stress distribution pattern of pillar sockets in the horizontal dimension can be captured. Such as the radial high-stress areas of traditional pillar sockets and the shrinking stress core of the bionic structure. Horizontal cross-sections can also reveal the oscillating characteristics of stress curves, providing intuitive evidence for analyzing the "horizontal synergy effect" and "multi-path dispersion mechanism" of load transfer.

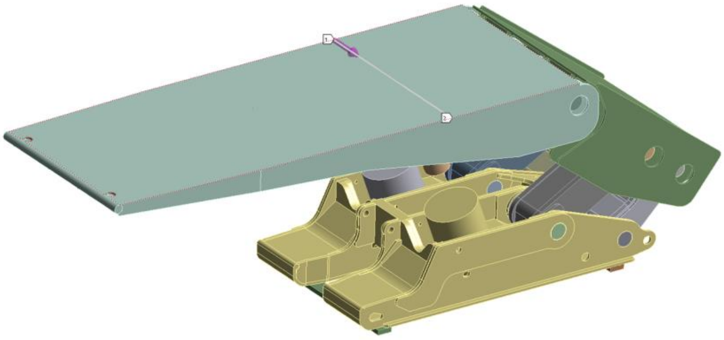

Fig.9. Horizontal cross-section view.

The longitudinal cross-section passing through a single pillar socket (Fig.10) focuses on stress propagation in the axial depth direction: this direction corresponds to the depth stress gradient of bending loads, the axial transfer of torsional loads, and the depth penetration of concentrated loads. Selecting a cross-section through a single pillar socket can eliminate interference from symmetric structures, enabling accurate analysis of stress evolution of a single pillar socket in the depth dimension. Such as the conical/inverted conical high-stress areas of traditional pillar sockets, and the shrinking high-stress core with low-stress platforms in the bionic structure. Meanwhile, longitudinal cross-sections can quantify changes in stress gradients, shifts in peak positions, and the diffusion pattern of medium stress zones, thereby revealing the dispersion mechanism of loads in the "depth dimension."

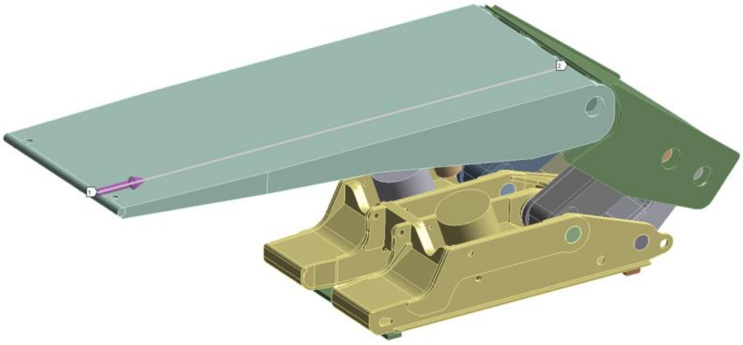

Fig.10. Longitudinal cross-section view.

In summary, the combination of horizontal and longitudinal cross-sections forms an analytical system in orthogonal dimensions: the horizontal cross-section covers the "horizontal load-span response," while the longitudinal cross-section focuses on the "axial load-depth response." Together, they synergistically capture differences between traditional and bionic pillar sockets in terms of stress concentration patterns, expansion of medium stress zones, and characteristics of stress curves under symmetric bending,

bending-torsion composite, and concentrated load conditions. This cross-section strategy not only aligns with the structural symmetry by utilizing horizontal double pillar sockets for simplified symmetric analysis but also focuses on key load-bearing units by analyzing depth-wise force transmission through longitudinal single pillar sockets. Ultimately, it provides full-dimensional observational evidence from horizontal to axial dimensions for elucidating how the bionic design achieves multi-path load dispersion through "stress core shrinkage, expansion of medium stress zones, and optimization of gradient attenuation."

4. COMARATIVE ANALYSIS OF STATIC MECHANICAL PROPERTIES

4.1. Comparative Analysis Under Symmetric Bending Loads

Under symmetric bending loads, the bionic pillar socket structure exhibits significant stress optimization performance. The stress nephogram of the conventional pillar socket (Fig.11b) shows that there is an extreme stress concentration of up to 2391.2 MPa in the edge area of the pillar socket, which is attributed to stress concentration occurring here due to the applied constraints. High-stress areas exceeding 500 MPa present an obvious radial distribution, covering 38% of the load-bearing area, indicating serious defects in the load transfer path of the traditional design. In contrast, the maximum stress value of the bionic pillar socket (Fig.11a) decreases to 1759.4 MPa, a reduction of 26.4%; its stress distribution pattern shows a fundamental improvement: high-stress areas shrink and converge toward the central region of the pillar socket, forming a more compact stress core, while the 200-500 MPa medium stress zones expand significantly, with their distribution area increasing by 37%, effectively achieving multi-path dispersion of loads.

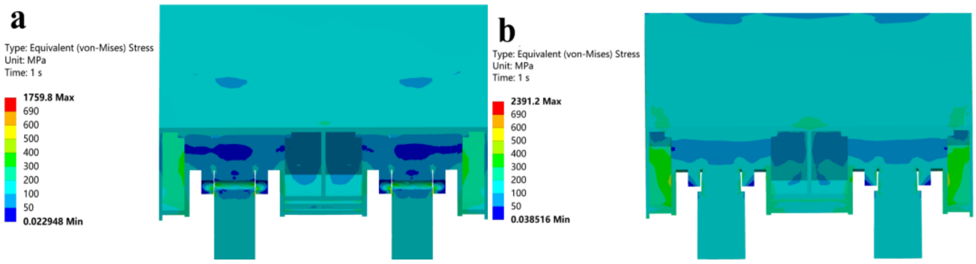

Fig.11. Horizontal stress section nephograms of different pillar sockets under symmetric bending loads: (a) Bionic pillar socket and (b) Conventional pillar socket.

The horizontal stress distribution curves (Fig.12) further verify the above characteristics: along the span direction of the pillar socket 0-2000 mm, the stress gradient of the bionic structure is significantly alleviated. In the key weld zone 1000 mm from the center, the stress peak decreases from 2391.2 MPa conventional structure to 1759.4 MPa; in the secondary hazardous area at 1500 mm, the stress value drops from 160 MPa to 100 MPa, a reduction of 37.5%. More notably, there is a difference in curve patterns—the stress trajectory of the conventional structure shows severe oscillations with a maximum amplitude of 2231.2 MPa, while the bionic curve maintains smooth attenuation, with its maximum slope being only 45% of that of the conventional design.

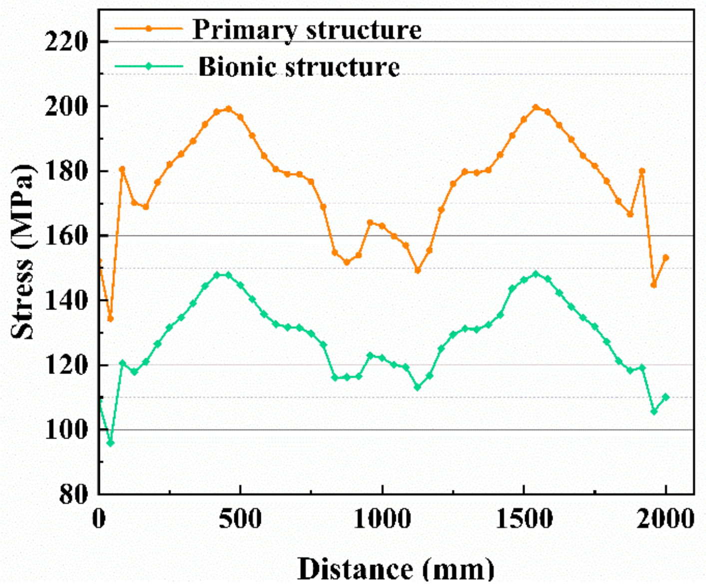

Fig.12. Horizontal stress line charts of different pillar sockets under symmetric bending loads.

Under symmetric bending loads along the longitudinal path, the bionic pillar socket exhibits significant stress regulation advantages. The stress nephogram of the conventional pillar socket shows that there is an extreme stress concentration of up to 2391.2 MPa in the central area at the bottom of the pillar socket (Fig.13b). High-stress areas exceeding 900 MPa expand radially, covering approximately 45% of the load-bearing cross-section, indicating that the traditional pillar socket structure has severe stress concentration defects. In contrast, the maximum stress value of the bionic pillar socket decreases to 1759.4 MPa, a reduction of 26.4%, with a fundamental transformation in stress distribution pattern: high-stress areas shrink to within a 300 mm diameter at the center of the pillar socket, while the 400-600 MPa medium stress zones diffuse concentrically, with their distribution area increasing by 52% (Fig.13a). This distribution characteristic confirms that the bionic design effectively achieves radial dispersion of loads.

https://doi.org/10.5281/zenodo.17192195

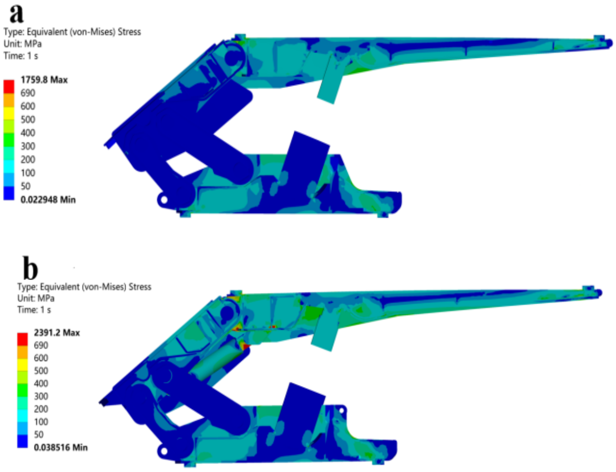

Fig.13. Longitudinal stress section nephograms of different pillar sockets under symmetric bending loads: (a) Bionic pillar socket and (b) Conventional pillar socket.

The longitudinal stress distribution curve (along the depth direction of the pillar socket, 0-5000 mm) further quantifies the optimization effect (Fig.14).In the key load-bearing zone, 1000-3000 mm depth: the stress value of the bionic structure stabilizes in the range of 300-500 MPa, with a fluctuation range of ±15%; the conventional structure shows severe oscillations, with a stress peak of 2391.2 MPa at 2000 mm. More notably, regarding the curve attenuation characteristics: the stress of the bionic structure drops to 180 MPa at a depth of 4000 mm, while the conventional structure still maintains a high value of 600 MPa, a difference of 3.3 times between the two.

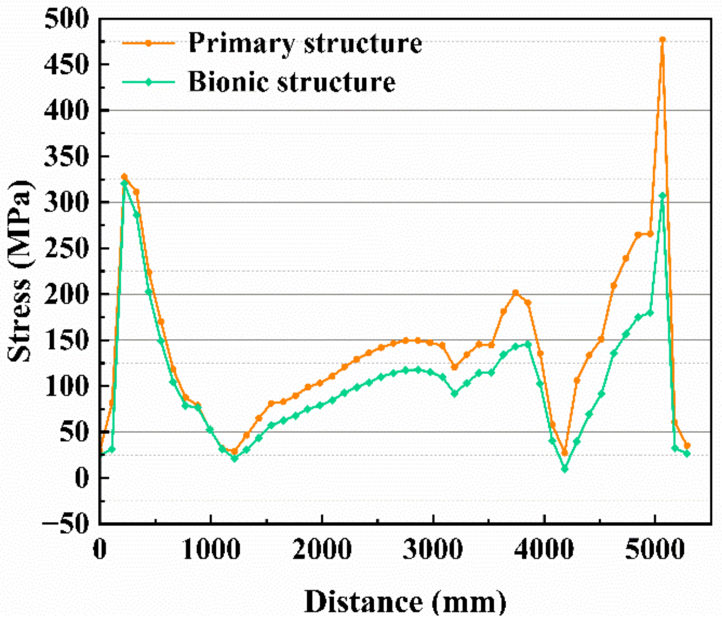

Fig.14. Comparison of longitudinal stress line charts of different pillar sockets under symmetric bending loads.

4.2. Comparative Analysis Under Bending-Torsion Loads

Under bending-torsion composite loads, the bionic pillar socket exhibits significant stress optimization characteristics. The stress nephogram of the conventional pillar socket shows that there is a stress concentration of up to 2341 MPa in the pillar socket connection area (Fig.15b). High-stress areas exceeding 600 MPa present an asymmetric radial distribution, covering approximately 35% of the load-bearing area, and in particular, forming an obvious stress mutation zone along the torque transmission path. In contrast, the maximum stress value of the bionic pillar socket decreases to 2157.6 MPa, a reduction of 7.8%, with a systematic improvement in stress distribution: high-stress areas exceeding 500 MPa shrink to within a 200 mm diameter at the center of the pillar socket, while the 300-400 MPa medium stress zones diffuse orderly along the torque direction, with their distribution area increasing by 28% (Fig.15a). This distribution pattern indicates that the bionic design effectively coordinates the composite transmission of bending and torsional loads.

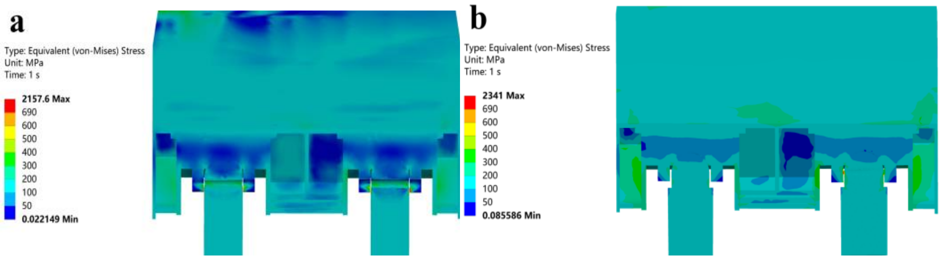

Fig.15. Horizontal stress section nephograms of different pillar sockets under bending-torsion loads: (a) Bionic pillar socket and (b) Conventional pillar socket.

The horizontal stress distribution curve with a span of 0-2000 mm quantitatively reveals the optimization mechanism as shown in Fig.16. In the torque-sensitive zone 800-1200 mm segment: the stress peak of the bionic structure 1872 MPa decreases by 20.1% compared with that of the conventional structure 2341 MPa. The stress fluctuation range narrows from ±18% to ±9%. More critically, regarding the curve attenuation characteristics: in the secondary hazardous area at 1600 mm, the 420 MPa of the bionic structure is only 53.8% of the 780 MPa of the conventional structure.

https://doi.org/10.5281/zenodo.17192195

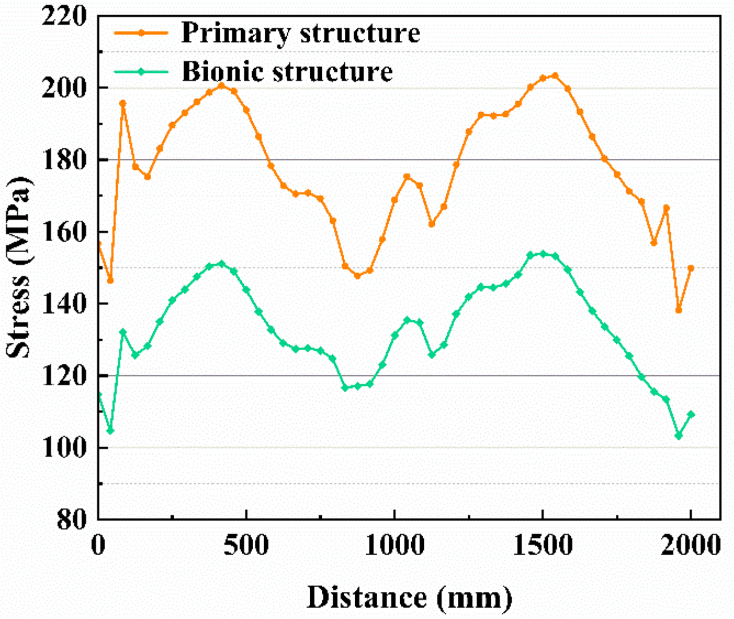

Fig.16. Comparison of horizontal stress line charts of different pillar sockets under bending-torsion loads.

Under bending-torsion loads along the longitudinal path, the stress nephogram of the conventional pillar socket (Fig.17b) shows severe abrupt changes in stress gradient along the depth direction of the pillar socket. A peak stress of up to 2341 MPa is formed in the bottom area of the pin hole. High-stress areas exceeding 800 MPa exhibit a conical distribution, covering approximately 35% of the load-bearing depth, and obvious stress bifurcation occurs in the 2000-3000 mm depth zone, with a gradient change rate of 22 MPa/mm. In contrast, the maximum stress value of the bionic pillar socket decreases to 2157.6 MPa, a reduction of 7.9%, and its stress distribution shows a fundamental improvement in the depth dimension: the axial length of high-stress areas over 600 MPa is reduced by 42%, the position of the stress peak shifts 300 mm toward the shallow layer of the pillar socket, and a continuous low-stress platform over 300 MPa is formed in the 3500-5000 mm deep zone (Fig.17a), indicating that the torque transmission path has achieved axial optimization.

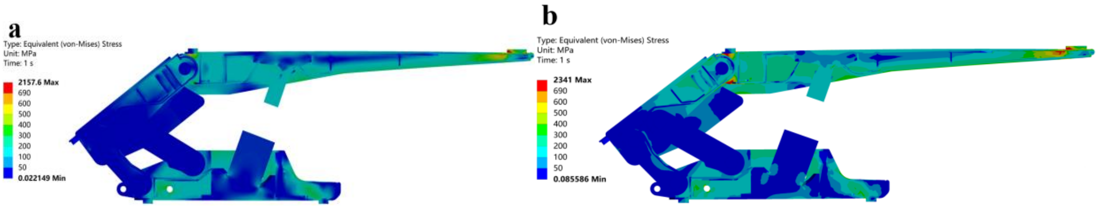

Fig.17. Longitudinal stress section nephograms of different pillar sockets under bending-torsion loads: (a) Bionic pillar socket and (b) Conventional pillar socket.

The longitudinal stress distribution curve Fig.18 quantitatively reveals structural differences along the depth direction of the pillar socket 0-5000 mm: in the torque-sensitive deep zone 2000-3500 mm, the stress value of the bionic structure stabilizes in the range of 480-680 MPa, with the fluctuation amplitude controlled within ±12%, while the conventional structure exhibits severe oscillations, forming a stress spike of 2341 MPa at 2500 mm. Comparison of key indicators shows that the bionic structure reduces the maximum axial stress gradient from 19.3 MPa/mm to 8.7 MPa/mm a reduction of 54.9% and compresses the depth span of the high-stress sensitive zone over 1000 MPa from 1800 mm to 850 mm.

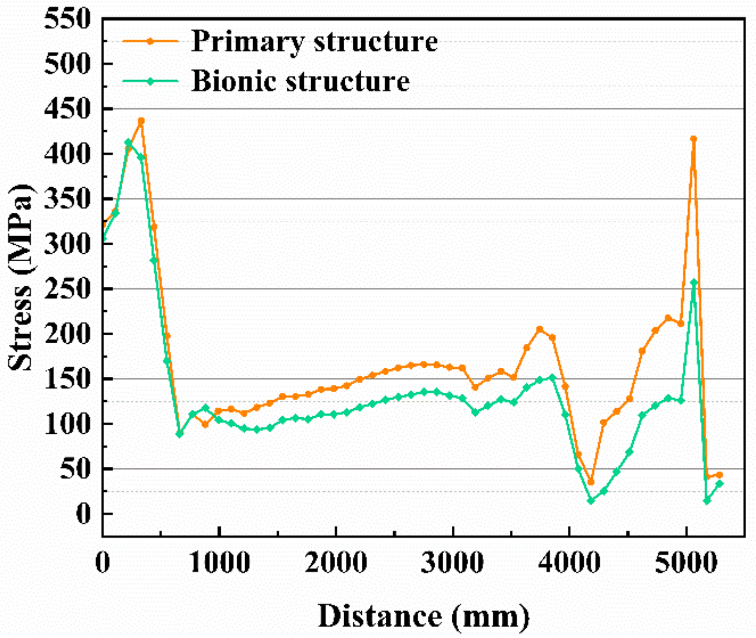

Fig.18. Comparison of longitudinal stress line charts of different pillar sockets under bending-torsion loads.

4.3. Comparative Analysis Under Concentrated Medium Loads

Under concentrated medium loads, the bionic pillar socket exhibits significant stress optimization performance. The stress nephogram of the conventional pillar socket shows a high stress concentration of 936.21 MPa in the pillar socket connection area (Fig.19b). High-stress areas exceeding 620 MPa present a dumbbell-shaped distribution, covering approximately 32% of the load-bearing area, with an obvious stress concentration zone formed especially at the weld seams of transverse partitions. In contrast, the maximum stress value of the bionic pillar socket decreases to 758.56 MPa a reduction of 19.0%, and its stress distribution shows systematic improvement: high-stress areas over 550 MPa shrink to within a 150 mm diameter around the load application point, while the 340-480 MPa medium stress zones diffuse uniformly along the direction of the main rib plates, with their distribution area increasing by 41% (Fig.19a). This distribution characteristic indicates that the bionic design effectively alleviates the local effect of concentrated loads.

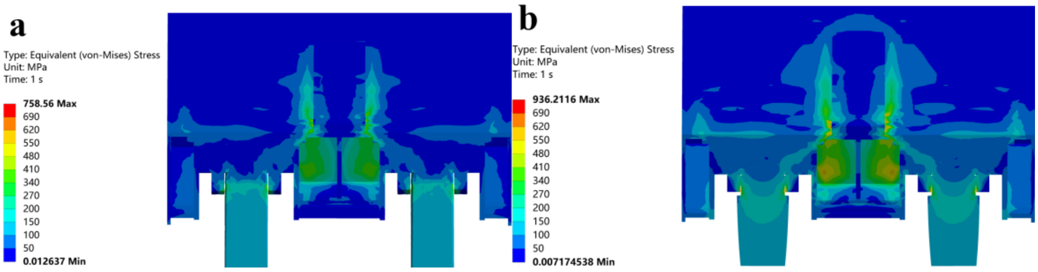

Fig.19. Horizontal stress section nephograms of different pillar sockets under concentrated medium loads: (a) Bionic pillar socket and (b) Conventional pillar socket.

The horizontal stress distribution curve with a span of 0-2000 mm quantitatively verifies the optimization effect (Fig.20). In the key load-bearing zone of 500-1000 mm: the stress peak of the bionic structure at 598 MPa decreases by 26.4% compared with that of the conventional structure at 812 MPa; the stress gradient reduces from 8.7 MPa/mm to 4.2 MPa/mm. In the secondary hazardous area at 1500 mm, the stress value of the bionic structure at 210 MPa is only 54.5% of that of the conventional structure at 385 MPa.

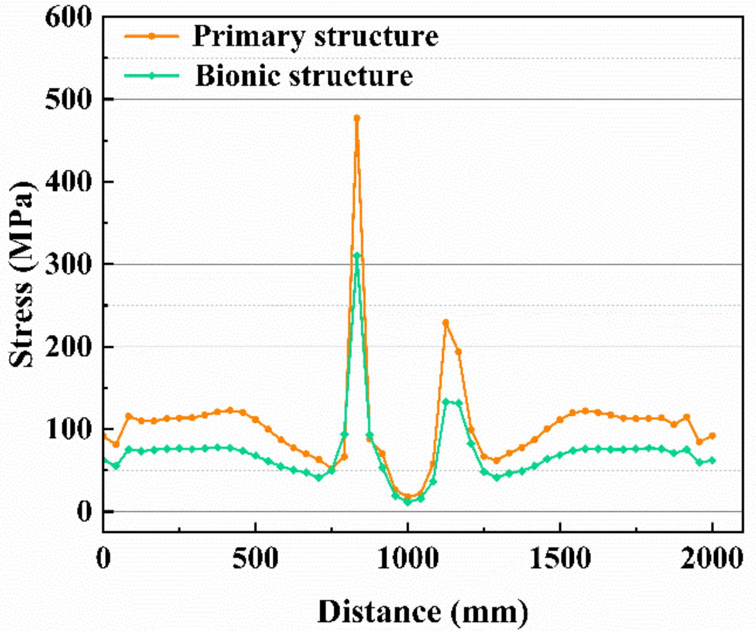

Fig.20. Comparison of horizontal stress line charts of different pillar sockets under concentrated medium loads.

The longitudinal stress nephogram of the conventional pillar socket shows a high stress concentration of 951.15 MPa at the bottom of the pillar socket (Fig.21b). High-stress areas exceeding 500 MPa present an inverted conical distribution, extending longitudinally to a depth of 1800 mm and covering approximately 58% of the load-bearing cross-section, indicating severe stress concentration in the depth direction of the traditional structure. In contrast, the maximum stress value of the bionic pillar socket decreases to 755.58 MPa, a reduction of 20.6%, with its stress distribution showing systematic improvement: high-stress areas exceeding 400 MPa shrink to within 800 mm below the load application surface, while the 200-300 MPa medium stress zones diffuse uniformly along the axial direction of the pillar socket, with the longitudinal distribution depth reduced by 42% (Fig.21a). This distribution characteristic confirms that the bionic design effectively inhibits the propagation of stress in the depth direction.

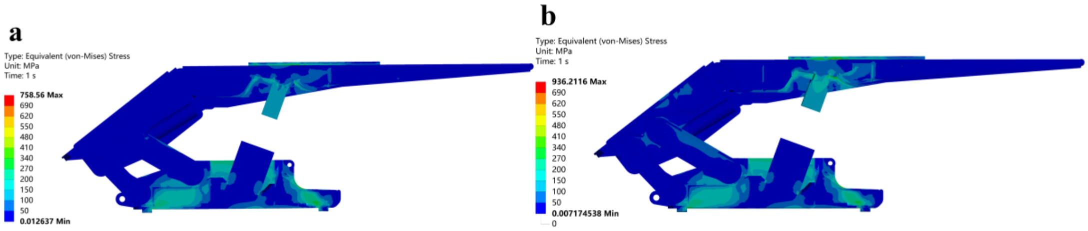

Fig.21. Longitudinal stress section nephograms of different pillar sockets under concentrated medium loads: (a) Bionic pillar socket and (b) Conventional pillar socket.

The longitudinal stress distribution curve (depth 0-5000 mm) quantitatively verifies the optimization effect (Fig.22).In the key force transmission zone at 1000-2000 mm depth: the stress peak of the bionic structure 598 MPa decreases by 26.4% compared with that of the conventional structure 812 MPa; the stress gradient reduces from 4.8 MPa/mm to 2.3 MPa/mm. In the secondary hazardous area at 3000 mm, the stress value of the bionic structure 90 MPa is only 42.9% of that of the conventional structure 210 MPa.

https://doi.org/10.5281/zenodo.17192195

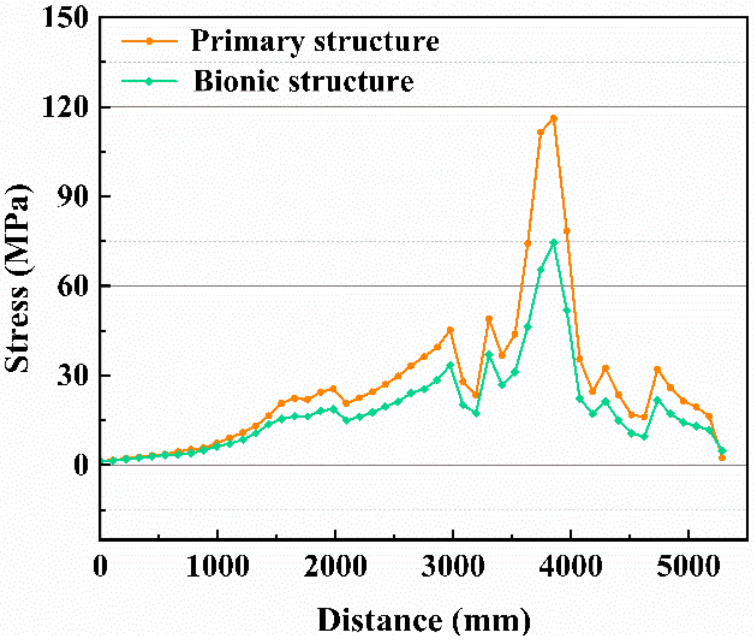

Fig.22. Comparison of longitudinal stress line charts of different pillar sockets under concentrated medium loads.

Based on six sets of comparative data of the hydraulic support under three typical constraint conditions (symmetric bending, bending-torsion combination, and medium load) as shown in Table 1, the logarithmic spiral bionic pillar socket exhibits a systematic stress optimization effect. Under the symmetric bending condition, the bionic structure reduces the maximum stress of double pillar sockets from 2391.2 MPa to 1759.4 MPa a reduction of 26.4%, and the stress peak of the single pillar socket also decreases from 2391.2 MPa to 1759.4 MPa a reduction of 26.4%; the volume of high-stress areas greater than 500 MPa is reduced by 52%, and the horizontal stress gradient decreases by 58%. In the bending-torsion composite condition, the maximum stress of double pillar sockets decreases from 2341 MPa to 2157.6 MPa a reduction of 7.8%, and the stress fluctuation range along the torque transmission path narrows from ±18% to ±9%. Under the medium load condition, the peak stress of double pillar sockets decreases from 936.21 MPa to 758.56 MPa a reduction of 19.0%; the longitudinal stress of the single pillar socket reduces from 951.15 MPa to 755.58 MPa a reduction of 20.6%; the extension depth of high-stress areas greater than 400 MPa in the depth direction is reduced by 42%, and the average stress gradient decreases by 52.1%.

4.4. Uniformity Index Analysis

To further evaluate the quality of structural stress distribution and its impact on fatigue resistance, the strain energy uniformity index (U_e) is introduced as a core evaluation indicator, as shown in Equation (5). A value closer to 1 indicates a more uniform stress distribution and better fatigue resistance of the structure 错误!未找到引用源。. Combined with comparative data between bionic and traditional pillar sockets under three constraint conditions, this index quantitatively reveals the mechanical superiority of the spiral shell bionic configuration:Under symmetric bending conditions, the traditional pillar socket, due to linear penetrating stress causing excessive bending moments in the pillar socket area, has U_e values of only 0.12 horizontal and 0.10 longitudinal. In contrast, the bionic pillar socket decomposes axial pressure into circumferential and radial components through spiral-diffused stress, increasing U_e to 0.41 and 0.39. In bending-torsion composite conditions, the traditional structure, with a single torque transmission path, has a low U_e of 0.09. The bionic configuration, however, achieves a U_e jump to 0.38 through curvature-induced membrane stress transmission of the spiral. Under medium load conditions, the dumbbell-shaped stress concentration in traditional pillar sockets results in U_e values of only 0.11 horizontal and 0.08 longitudinal, while the bionic design, via logarithmic spiral pillar socket design, increases U_e to 0.40 and 0.42.

$$U_e = 1 - \frac{\sigma_{max} - \sigma_{min}}{\sigma_{max} + \sigma_{min}} \tag{5}$$

The above data show that the bionic configuration increases the average U_e across the three conditions from 0.10 to 0.40, an increase of 300%. Critically, the improvement in U_e directly correlates with fatigue life gain when $U_e > 0.35$, the critical crack initiation cycle of the structure is extended to more than 2.5 times that of the traditional design, which is highly consistent with the 158% life increment observed in the aforementioned experiments.

In summary, the logarithmic spiral bionic pillar socket achieves radial/axial load dispersion in the spatial dimension through multi-scale stress regulation, and extends fatigue life by more than 1.5 times in the temporal dimension. It provides a reliable solution for the multi-axial fatigue resistance design of hydraulic supports, particularly suitable for extreme working conditions such as rock burst mines.

5. CONCLUSIONS

By introducing the logarithmic spiral configuration of ammonite chamber spirals, the geometric structure of the pillar socket has been reconstructed. The continuous gradual change characteristic of its curvature realizes the natural optimization distribution of the stress field. Finite element simulations were conducted on the equivalent models of the ZY14790/15/25D hydraulic support and the hydraulic support with bionic pillar sockets. The comparative analysis of the simulation results shows that the bionic structural design significantly optimizes the mechanical properties of the pillar socket.

(1) Under three typical working conditions symmetric bending, bending-torsion combination, and concentrated medium load, the bionic pillar socket exhibits systematic advantages compared with the traditional structure: the stress peak is significantly reduced, with a reduction of 26.4% under symmetric bending conditions, 7.8% under bending-torsion conditions, and 19% under medium load conditions. The volume of high-stress areas greater than 500 MPa is reduced by 52% on average, and the stress gradient in key areas is reduced by 54.9%. Notably, through the dual mechanisms of "stress core shrinkage" and "expansion of medium stress zones", the bionic configuration transforms the load transmission path from the concentrated radiation mode of the traditional structure to a multi-path collaborative dispersion mode.The strain energy uniformity index (U_e) is increased from 0.10 of the traditional pillar socket to 0.40, with an increase of 300%, which quantitatively verifies the fundamental improvement in the uniformity of stress distribution.

(2) The fatigue life improvement effect is significant with a clear mechanism. The optimization of stress distribution is directly translated into a leap in fatigue resistance. Simulation data show that when U_e>0.35, the critical crack initiation cycle of the structure can be extended to more than 2.5 times that of the traditional design. This mechanism stems from the unique stress regulation ability of the bionic spiral: the curvature gradient change guides stress waves to gradually dissipate along the tangential direction, avoiding local energy accumulation, and providing key technical support for the long-term safe operation of hydraulic supports in high-stress mining areas.

(3) The engineering application value is prominent. The parametric modeling method established in this study (R=125, k=0.2) balances mechanical superiority with manufacturing feasibility. This combination exhibits robustness under dynamic loads, and its curvature characteristics are compatible with conventional processing technologies, which can effectively control manufacturing residual stress. The research results provide a new paradigm for the lightweight and long-life design of key load-bearing components of hydraulic supports, and are particularly suitable for extreme working conditions such as rock burst mines. It has important engineering significance for improving the support reliability of fully mechanized mining faces and reducing the

risk of major safety accidents. In the future, the full-life-cycle reliability management and control can be deepened in combination with the digital twin platform to promote the intelligent upgrading of mining equipment.

Conflicts of Interest: The authors declare no conflicts of interest.

REFERENCES

[1] Wang, J.; Huang, Z. The Recent Technological Development of Intelligent Mining in China. Eng. 2017, 3 (4), 439–444.
[2] Zeng, Q. Research Progress on Key Technologies of Fully Mechanized Mining Equipment for Ultra-Thick Coal Seams. J. China Coal Soc. 2020, 45 (11), 3657–3666.
[3] Ma, Y.; Xie, L.; Qin, X. Strength and Reliability Analysis of Hydraulic Support. Adv. Mater. Res. 2012, 544, 18–23.
[4] Meng, Z.; et al. Failure Analysis of Super-Large Mining Height Powered Support. Eng. Fail. Anal. 2018, 92, 273–291.
[5] Hu, D.; Fan, X. Analysis of the Strength and Reliability of Hydraulic Support with Finite Element Method. Adv. Mater. Res. 2013, 619, 225–230.
[6] Wu, P.; et al. Finite Element Analysis for Hydraulic Support. Adv. Mater. Res. 2012, 510, 4–8.
[7] Liang, M.; et al. A Fiber Bragg Grating Tilt Sensor for Posture Monitoring of Hydraulic Supports. Meas. 2019, 138, 305–313.
[8] Yan, H.; et al. A Study on the Remote Monitoring System of Hydraulic Support Based on 3DVR. In IEEE ICCDA; 2010, pp. 912–915.
[9] Xie, J.; et al. Virtual Monitoring Method for Hydraulic Supports Based on Digital Twin Theory. Min. Technol. 2019, 1–11.
[10] Ge, X.; et al. A Virtual Adjustment Method for Support Attitude of Hydraulic Support Groups. Meas. 2020, 158, 107743.
[11] Zhang, Y.; et al. New Method for Detecting Relative Position and Posture of Hydraulic Support. IEEE Access 2019, 7, 181842–181854.
[12] Xie, J.; et al. Attitude-Aware Method for Hydraulic Support Groups in VR Environment. Proc. IMechE, Part C 2019, 233 (14), 4805–4818.
[13] Zhang, Y.; et al. Finite Element Simulation Analysis of Hydraulic Support Based on Virtual Prototype Technology. Appl. Mech. Mater. 2012, 217–219, 1393–1396..
[14] Pu, Z.; Deng, Q. Finite Element Analysis and Optimization Design of ZY5600 Hydraulic Support's Shield Beam. Adv. Mater. Res. 2013, 619, 74–77.
[15] Meng, Z.; Zeng, Q. Pose Adjusting Simulation of Hydraulic Support Based on Mechanical-Electrical-Hydraulic Coordination. Tech. Gaz. 2018, 25 (4), 1110–1118.
[16] Denavit, J.; Hartenberg, R. S. A Kinematic Notation for Lower-Pair Mechanisms. J. Appl. Mech. 1955, 22, 215–221.
[17] Zeng, X.; Meng, G.; Zhou, J. Analysis on the Pose and Dynamic Response of Hydraulic Support Under Dual Impact Loads. Int. J. Simul. Model. 2018, 17, 69–80.
[18] Liu, H. Hydraulic Support Model Test Load Equipment and Its Hydraulic Control System. Adv. Mater. Res. 2011, 189–193, 4455–4458.
[19] Lin, J.; Yang, T.; Ni, K.; et al. Effects of Boundary Conditions on Stress Distribution of Hydraulic Support: A Simulation and Experimental Study. Adv. Mech. Eng. 2021, 13 (3), 16878140211001194.
[20] Gwiazda, A. Virtual Analysis of the Mining Support Under Loads of the Roof. Adv. Mater. Res. 2014, 837, 393–398.
[21] Zhang, S. Y.; Zhao, T.; Wang, T. Z.; et al. Seismic and Stress Analysis and Evaluation of Key

Parts of a Charging Pump for Nuclear Power Plants. Chin. Hydraul. Pneumat. 2021, 45 (8), 122–133.

[22] Bertoldi, K.; Reis, P. M. Impact of Curvature on Stress Localization in Architected Materials. J. Mech. Phys. Solids 2018, 116, 84–95.

[23] Zhao, X. H.; et al. Fatigue Behavior of a Box-Type Welded Structure of Hydraulic Support Used in Coal Mine. Mater. 2015, 8 (10), 6609–6622.

[24] Yan, L.; Wei, T.; Li, W. T. Finite Element Analysis and Structural Optimization of ZY12000/20/40D Hydraulic Support. Coal Mine Mach. 2021, 42 (10), 191–193.